Journal of Materials Chemistry A

Design of Trifunctional Catalysts for Promoting Sequential Condensation, Deoxygenation, and Aromatization of Pyrolyzed Mixed Waste

Journal:	*Journal of Materials Chemistry A*
Manuscript ID	TA-ART-03-2023-001368.R1
Article Type:	Paper
Date Submitted by the Author:	25-May-2023
Complete List of Authors:	Ahmed , Mohamed ; The University of Queensland - Saint Lucia Campus, Batalha, Nuno; IRCELYON, Chemical Engineering Karim, Rezaul; King Saud University, Center of Excellence for Research in Engineering Materials, Faculty of Engineering Alnaser, Ibrahim; King Saud University, Mechanical Engineering Yamauchi, Yusuke; University of Queensland, Chemical Engineering Kaneti, Yusuf; The University of Queensland, Australian Institute for Bioengineering and Nanotechnology Konarova, Muxina; University of Queensland, University of Queensland

Design of Trifunctional Catalysts for Promoting Sequential Condensation, Deoxygenation, and Aromatization of Pyrolyzed Mixed Waste

Mohamed HM Ahmed[a], Nuno Batalha[a,b], Mohammad Rezaul Karim[c], Ibrahim Abdullah Alnaser[c], Yusuke Yamauchi[d, e], Yusuf Valentino Kaneti[d]*, Muxina Konarova[a]*

[a] *School of Chemical Engineering, The University of Queensland, Brisbane, Australia*

[b] *Université de Lyon, Institut de Recherches sur la Catalyse et l'Environnement de Lyon (IRCELYON), UMR5256 CNRS-UCB Lyon 1, 2 Avenue Albert Einstein, 69626, Villeurbanne Cedex, France*

[c] *Department of Mechanical Engineering, College of Engineering, King Saud University, Riyadh 11421, Saudi Arabia*

[d] *Australian Institute of Bioengineering and Nanotechnology, The University of Queensland, Brisbane, Australia*

[e] *Department of Materials Process Engineering, Graduate School of Engineering, Nagoya University, Nagoya 464–8603, Japan*

*__Corresponding authors:__ m.konarova@uq.edu.au, v.kaneti@uq.edu.au

Abstract

The upgrading of bio-oil often leads to significant carbon losses due to excessive decarboxylation and decarbonylation. However, this may be alleviated by deploying an innovative multi-functional catalyst that promotes C−C coupling while catalyzing deoxygenation/hydrodeoxygenation reactions. In this work, we develop trifunctional catalysts by consecutive post-synthesis treatments of commercial ZSM-5 catalyst (ZSM-comm). These treatments include impregnation of alkaline metal (magnesium) followed by temporary pore blocking with CTAB prior to the growth of SBA-15 using P123 as a template and transition/noble metal salts (nickel nitrate and platinum chloride). The prepared trifunctional catalysts exhibit three active sites, namely acidity, basicity, and reducibility as confirmed by NH_3-TPD, CO_2-TPD, and TPR measurements. The integration of the three active sites results in a remarkable increase in oil yield from 4.9% over ZSM-comm to 17.1 and 13.5% over Mg-Ni/meso-ZSM and Mg-Pt/meso-ZSM catalysts, respectively. These trifunctional catalysts also exhibit enhanced selectivity toward alkenes and alkanes in oil, which increases from 7.6% over ZSM-comm to 26.3 and 19.6% over Mg-Ni/meso-ZSM and Mg-Pt/meso-ZSM, respectively. The oxygenates (phenols, furans, acids, and ketones) also show an apparent shift in the carbon number toward the fuel range (C5-C13), suggesting the occurrence of C−C coupling. Additionally, the trifunctional catalysts help in increasing the selectivity toward monocyclic aromatic hydrocarbons (MAHs) from 75.2 to 93.7%.

1. Introduction

Securing sustainable energy resources is of the utmost importance in preventing global warming, which poses a tremendous challenge to nations worldwide. In the race to achieve zero carbon emissions, all current green resources must ultimately be exploited to eliminate waste and pollution.[1, 2] Municipal solid waste (MSW) has a high energy density, yet it continues to be landfilled in most countries. However, the valorization of MSW can contribute to the sustainability of the existing energy pool. Through fast pyrolysis, for instance, MSW can be transformed into a crude bio-oil with the potential to be refined into liquid fuels via hydrotreatment.[3, 4] However, due to the complicated chemical structure of the bio-oil produced from MSW pyrolysis, the process of upgrading this crude oil is challenging and costly.[5]

Fast pyrolysis is the thermal decomposition of polymeric materials at elevated temperatures. Typically, fast pyrolysis can be observed at temperatures between 400 and 550 ˚C, which are also suitable for the upgrading process of volatiles. Hence, thermal pyrolysis and catalytic upgrading can take place within the same reactor, thus conserving energy and significantly improving the quality of the obtained bio-oil.[6, 7] By utilizing this strategy, it is feasible to capitalize on the synergy that exists between the materials (biomass and plastics) found in MSW. For example, the plastic waste in MSW can be used as a source of hydrogen for in-situ oil upgrading by catalytic transfer hydrogenation of pyrolysis vapors. Thus a multifunctional catalyst is required that is able to promote several reactions simultaneously during the pyrolysis.[8] The ZSM-5 catalyst has been extensively studied in the pyrolysis of long-chain polymeric and biomass macromolecules, however it often leads to low oil yield.[9-11] Indeed, the acidic sites in ZSM-5 zeolite, particularly the Brønsted sites[12], favour cracking reactions, which increase gas-phase products and minimize the bio-oil carbon yield (liquid phase). However, the incorporation of alkaline earth metals in the catalyst has been demonstrated to have a positive impact on bio-oil yield.[13] In addition to the benefits of alkaline earth metals in C−C coupling[14, 15], they also enhance the deoxygenation.[16] Bifunctional (acidic/basic) zeolites are, therefore, have been the subject of numerous studies, however, the size of these cations is reported to be hindering the diffusion path through the pore channels.[17, 18] In parallel to alkaline metals, zeolites modified with transition metals have also been studied in depth and have been found to exhibit hydrogen transfer and aromatization abilities.[19, 20] For instance, transition metals, such as nickel (Ni) and cobalt (Co), can further promote deoxygenation and

aromatization, making them especially attractive for co-pyrolysis applications. However, the oxygen removal process over Ni and Co results in excess CO_2 and CO, which causes a substantial loss in bio-oil yield.[21, 22]

Studies focusing on the fabrication of catalysts that integrate zeolite, alkaline, metal, and transition metal in one composite, thus combining the advantages of each type of active phase, *i.e.*, acid, base, and metal, respectively, are lacking in the literature. Indeed, synthesizing such materials is a significant challenge since it is necessary to position the alkaline and transition metals on the zeolite surface without sacrificing or disabling its unique catalytic and structural properties, *i.e.*, active site poisoning and pore blockage.[23] Alternatively, the highly reactive pyrolysis products can lead to coke formation inside the zeolite microporous framework, hence limiting access to the active sites. Such effects can be counteracted by including mesoporosity in the catalyst, which minimizes coke formation and facilitates diffusion limitation that many long-chain polymeric derivatives and bulky sugar molecules encounter in the micropores of ZSM-5.[24-29] Furthermore, the mesopores on zeolite catalysts can be used to deposit other active phases, such as alkaline or transition metals, thereby avoiding pore blockage and promoting the catalytic cascade effect.[30, 31]

In this study, we synthesize a trifunctional catalyst which can promote sequential condensation, deoxygenation, and aromatization of pyrolyzed mixed waste by modifying commercial ZSM-5 catalyst with mesoporous silica and Mg (as the alkaline metal), Ni (as the transition metal) or Pt (as the noble metal). To overcome the potential diffusion blockage that may occur with the integration of metals into the zeolite surface, a unique synthesis method is developed which facilitates the growth of mesoporous silica (SBA-15) on the ZSM-5 crystals. The selective deposition of the metals (Pt or Ni) on the mesoporous silica is possible through the combined use of CTAB and mild coking treatment which temporarily block the micropore channels in ZSM-5, which are ultimately regenerated through calcination. The use of these multifunctional catalysts for the pyrolysis of mixed plastic and biomass feedstocks permits increased carbon recovery, while also producing a high-quality oil.

2. Experimental Section

2.1. Catalyst synthesis

Commercial ZSM-5 (NH_4-ZSM-5 - CBV 2314) purchased from Zeolyst international was used as the parent catalyst. Before use, the as-purchased zeolite was calcined at 550 ˚C for 5 h to obtain H-ZSM-5. Magnesium was first introduced to H-ZSM-5 by wet impregnation in which 1.2 mmol of magnesium nitrate hexahydrate ($Mg(NO_3)_2 \cdot 6H_2O$, 99%, Sigma Aldrich) was dissolved in 3 mL of deionized water. This solution was added dropwise to 3 g of H-ZSM-5. The resulting paste was left to dry overnight before being moved to a muffle furnace. Afterward, the impregnated sample was calcined in a muffle furnace at 550 ˚C for 5 h. The resulting catalyst was referred to as Mg/H-ZSM-5.

Before growing the mesoporous silica on the Mg/H-ZSM-5, the inner micropore channels of ZSM-5 were blocked using CTAB ($C_{19}H_{42}BrN$, ≥99%, Sigma Aldrich). Typically, 0.41 mmol of CTAB was dissolved in 3 g of ethanol, and the formed solution was used to impregnate 3 g of Mg/H-ZSM-5. The sample was dried overnight and then thermally treated at 250 ˚C for 2 h. The sample colour changed from the typical white colour of zeolite to greyish colour, indicating partial coking caused by the CTAB inside the microporous channels. This sample was referred to as Mg-CTAB/ZSM.

The procedure for growing mesoporous silica (SBA-15) on zeolite (ZSM-5) started with the preparation of a solution composed of 4.8 g of Pluronic P123 (Sigma Aldrich) and 72 mL of distilled water. The solution was stirred at 40 °C for 1 h until the surfactant was homogeneously dispersed. Following this, 0.2 g of aluminium isopropoxide ($C_9H_{21}O_3Al$, ≥98%, Sigma Aldrich) was added to the solution, followed by the addition of 13 mL of tetraethyl orthosilicate ($SiC_8H_{20}O_4$, 40 wt.%, Sigma Aldrich). After 1 h, 1.0 mmol of nickel nitrate hexahydrate ($Ni(NO_3)_2 \cdot 6H_2O$, 99%, Sigma Aldrich) or 1.0 mmol of platinum (IV) chloride ($PtCl_4$, 96%, Sigma Aldrich) was introduced to the solution. The solution was stirred for 20 h, and, finally, 3 g of Mg-CTAB/ZSM was added. The solution was left under stirring for another 3 h before it was transferred to a Teflon-lined stainless steel autoclave. The sample was kept in the oven for 48 h at 180 °C before it was washed and dried. The organic templates were removed by calcining the catalyst at 600 °C for 5 h in a muffle furnace. The sample prepared without the addition of Mg, Pt, and Ni was denoted as Meso-ZSM and the samples containing metals were named as Mg/meso-ZSM, Mg-Ni/meso-ZSM, and Mg-Pt/meso-ZSM.

2.2. Catalyst characterization and bio-oil analysis

The composition andcrystallinity of the catalysts were analyzed using X-ray diffractometer. X-ray diffraction patterns were collected by Rigaku Miniflex equipped with a 9 kW Cu rotating anode source. The relative crystallinity was calculated by comparing the peak height of the 2θ at 7.9, 8.9, and 23.2° of the catalyst to that of commercial ZSM-5. The scanning electron microscopy (SEM) images were captured by JEOL 7001 instrument fitted with a secondary electron detector. A transmission electron microscope (TEM) was also deployed to observe the mesoporosity and the location of the metals using Hitachi HT7700 operated at 120 kV. A Micromeritics ASAP2020 apparatus was used to determine the catalyst's porosity. The machine generated the nitrogen-adsorption-desorption isotherms to calculate the surface and pore size distribution using the BET and DFT models, respectively.

The multiple active sites of the catalyst were measured using ASAP2029 equipped with a thermal conductivity detector (TCD). Before the NH_3-TPD and CO_2-TPD experiments, 100 mg of the catalyst was heated to 550 °C under helium flow (50 ml/min) to remove moisture and any adsorbed organics. The sample was later cooled to 100 °C in which a flow of pure NH_3 or CO_2 (10 mLmin) was passed through the sample for 20 min. After the probe molecule flow was stopped, the sample was purged with helium (50 ml/min) for 10 min. With continuous helium flow, the sample's temperature was elevated at a heating rate of 5 °C/min to 800 °C while the TCD signal was recorded. Temperature-programmed reduction (TPR) experiments followed a similar protocol to that of TPD by using a 5 wt.% H_2 in N_2 mixture (50 ml/min) to reduce the samples. The reduction program was set from 50 °C to 600 °C with a heating rate of 5 °C/min. The optical absorption spectra of the samples were obtained using a Shimadzu UV-3100 PLUS spectrophotometer. High-resolution transmission electron microscope (HRTEM), Hitachi HF5000, was used to study the size and location of the metals. The instrument was equipped with probe-forming lens systems that featured a spherical aberration corrector (Cs). X-ray Photoelectron Spectroscopy (XPS) was conducted using the Kratos Axis Ultra photoelectron spectrometer equipped with mono Al Kα (1486.6 eV) X-rays.

The bio-oil obtained from co-pyrolysis was analyzed using a Shimadzu TX8050 NX gas chromatography equipped with an Agilent J&W DB-5 column. The bio-oil sample was diluted with acetone by dissolving 15 mL of the oil in 1000 mL of acetone. The injection mode used was split with a 20 split ratio

and the injection temperature was maintained at 250 °C. The oven temperature was initially set at 40 °C for 1.5 min and then increased to 110 °C with a ramping rate of 8 °C/min. Finally, the oven temperature was raised to 250 °C with a heating rate of 6 °C/min and kept for 1 min.

2.3. Co-pyrolysis reaction

A fixed-bed reactor was used to assess the catalytic performance of all the catalysts. The reactor design and dimensions were previously reported.[26] The ratio of catalyst to feedstock is maintained at 1:1 in all experiments. After each experiment, the condenser usually contained three different types of products, namely water, wax, and oil. Water and oil are inseparable due to the small quantities, thus they are recovered together from the condenser. The wax then remained in the condenser where it was weighed and recorded. Karl-Fischer titrator was used to quantify the water content, hence the oil yield was also determined by the weight difference. The leftover inside the reactor was also collected and weighed. Next, the original weight of the catalyst was subtracted to obtain the solid, which represented char and coke. Gas was determined by the difference between the initial feedstock weight minus water, wax, oil, and solid.

3. Results and discussion

3.1. Catalysts characterization

3.1.1. Crystallinity and composition

The effects of post-synthesis treatments on the crystallinity of commercial ZSM-5 (ZSM-comm) are investigated using wide and low-angle XRD, as shown in **Fig. 1**. From **Fig. 1a**, it can be observed that the characteristic XRD pattern of MFI zeolite is present in all samples, indicating that the crystalline structure of ZSM-5 is maintained throughout the modification steps. Nonetheless, the MFI characteristic peaks are less intense on the modified ZSM-5 catalysts compared to ZSM-comm, indicating the presence of an amorphous phase in these catalysts. The ratio between the intensity of the peaks of ZSM-comm (**Table 1**) and the remaining samples was used to assess the amount of crystalline zeolite in the samples, *i.e.*, the crystallinity. The relative crystallinity decreases with the introduction of mesoporous silica (SBA-15) to ZSM-comm with Meso-ZSM displaying a relative crystallinity of 67%, as seen in **Table 1**. This significant decline suggests that a large amount of amorphous silica is formed as a result of the incorporation of mesoporous silica. Indeed,

the elemental composition of Meso-ZSM reveals a significant increase in Si content, with the global Si/Al ratio being 21.3, against the Si/Al ratio of 11.7 for ZSM-comm (**Table 1**). Similarly, the low-angle XRD of Meso-ZSM unveils the presence of a new hump at ~0.7° belonging to (100) peak of SBA-15, thus confirming the existence of mesoporous silica in this sample (**Fig. 1b**).

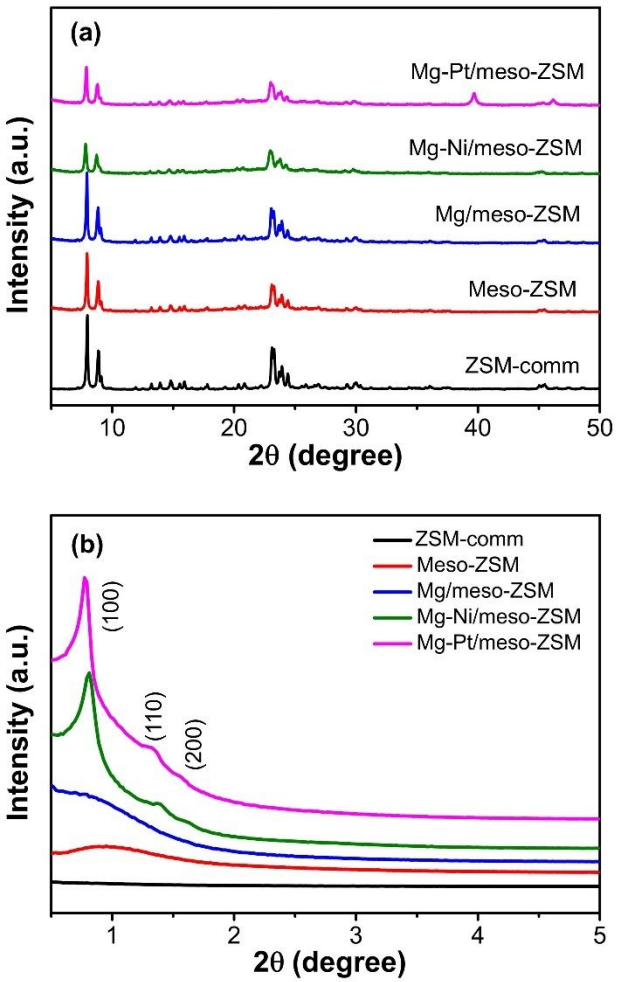

Fig. 1. (a) Wide-angle XRD and (b) low-angle XRD patterns of commercial and modified ZSM-5 catalysts.

Mg/meso-ZSM exhibits a higher relative crystallinity than Meso-ZSM, *i.e.*, 88% *vs.* 67%, respectively, suggesting less silica is deposited on this sample. In comparison, Mg/meso-ZSM displays a Si/Al ratio of 17.4, which is much lower than that of Meso-ZSM, again indicating that less silica is formed in this sample. Additionally, the low-angle XRD result suggests the presence of some silica but in a different orientation to Meso-ZSM. The broad peak, which is centered at 1.3°, indicates the creation of disordered mesoporous silica.[32] The only difference in preparation between Meso-ZSM and Mg/meso-ZSM is that the latter includes an extra Mg impregnation step followed by drying and calcination at 550 °C. Thus, Mg/meso-ZSM contains

0.37 wt.% of Mg. However, the presence of Mg in the porous zeolite framework cannot explain the observed difference in the amount of SiO_2 deposited on the surface of the zeolite, since both Mg-Ni/meso-ZSM and Mg-Pt/meso-ZSM display similar crystallinity to Meso-ZSM, *i.e.*, 62%, 59%, and 67%, respectively, and contain Mg introduced using the same procedures as in Mg/meso-ZSM. Similarly, Mg-Ni/meso-ZSM, Mg-Pt/meso-ZSM, and Meso-ZSM display equivalent Si/Al ratios, *i.e.*, 22.8, 24.0, and 21.3, respectively. However, unlike Meso-ZSM, the low-angle XRD patterns of of Mg-Ni/meso-ZSM and Mg-Pt/meso-ZSM reveal the formation of the ordered SBA-15 silica phase (**Fig. 1b**), known by its distinctive three peaks at 0.8° (100), 1.4° (110) and 1.6° (200).[33] The addition of $Ni(NO_3)_2{\cdot}6H_2O$ or H_2PtCl_6 during the synthesis lower the pH of the solution which may favour the formation of SBA-15. It is worth mentioning here that the Mg loading comparably declines from 0.37% for Mg/meso-ZSM to 0.21 wt.% for Mg-Ni/meso-ZSM and 0.19 wt.% for Mg-Pt/meso-ZSM, which may be due to the higher silica formation.

Table 1. Crystallinity and elemental composition of the catalysts.

Catalyst	Relative crystallinity [%]	Si/Al[a]	Si/Ni[a]	Si/Pt[a]	Mg[a] [%wt.]	EFAl [%]
ZSM-comm	100	11.7	-	-	-	12.5
Meso-ZSM	67	21.3	-	-	-	19.9
Mg/meso-ZSM	88	17.4	-	-	0.37	8.70
Mg-Ni/meso-ZSM	62	22.8	215.2	-	0.21	10.7
Mg-Pt/meso-ZSM	59	24.0	-	15.1	0.19	9.90

a: determined by ICP-MS analysis (wt.%)

The wide-angle XRD pattern of Mg-Pt/meso-ZSM shows the emergence of two peaks at $2\theta = 39.8°$ and 46.5°, assigned to (111) and (200) peaks of metallic Pt, respectively.[34] This perfectly aligns with the ICP result, which shows the high Pt content (Si/Pt = 15) in this sample. It is important to mention that no characteristic peak of Ni is observed on Mg-Ni/meso-ZSM, which can be explained by the low concentration of Ni in this sample. Indeed, the Si/Ni ratio observed on Mg-Ni/meso-ZSM is 215, while the Si/Pt ratio of

Mg-Pt/Meso-ZSM is 15. Thus, Mg-Pt/meso-ZSM contains 4.3 times (molar-based) more metal than Mg-Ni/Meso-ZSM.

The analysis of the framework and extra framework aluminum (EFAl) in the samples was performed by ^{27}Al-NMR analysis (**Fig. 2**). As expected, two bands at around 0 and 55 ppm are observed, which can be ascribed to octahedral (EFAl) and tetrahedral (ZSM-5 framework) Al coordination, respectively.[35, 36] Based on the NMR peak area, the non-framework Al represents 12.5% of the total amount of Al in ZSM-comm, as seen in **Table 1**. This ratio rises to 19.9% in Meso-ZSM, indicating an increase in the EFAL contribution, which may be caused by the partial degradation of the zeolite framework during the treatment or to the deposition of Al species from the aluminium isoproxide present during the growth of mesoporous silica. In contrast, the amount of octahedral Al drops to around 10% when the SBA-15 phase is formed in Mg-Ni/meso-ZSM and Mg-Pt/meso-ZSM. This indicates the integration of Al into the zeolite framework (recrystallization) or partial removal of a part of the EFAl. It is important to mention that the $Ni(NO_3)_2{\cdot}6H_2O$ and H_2PtCl_6 salts decrease the pH of the synthesis solution and increase the solubility of $AlOH_x$ species.

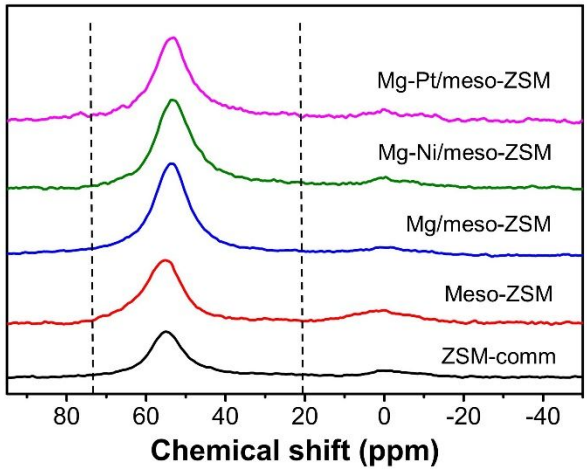

Fig. 2. ^{27}Al-NMR spectra of the catalysts.

3.1.2. Morphology and textural properties

The morphological and topological features of the catalysts were observed by SEM and TEM, as presented in **Figs. 3** and **S1**, respectively. ZSM-comm displays the typical block-like shape of ZSM-5 with sizes ranging between 0.5 and 1 μm (**Fig. 3a**). The TEM image of ZSM-comm (**Fig. S1a**) confirms that the sample contains no amorphous silica, as supported by the XRD result. In contrast, the presence of silica is very clear on Meso-

ZSM, as seen on the SEM and TEM images (**Figs. 3b** and **S1b**). In contrast, Mg/meso-ZSM shows only a small presence of silica based on the SEM and TEM images (**Figs. 3c** and **S1c**). This result is in good agreement with the above XRD and ICP results as the silica content is decreased in Mg/meso-ZSM relative to Meso-ZSM.

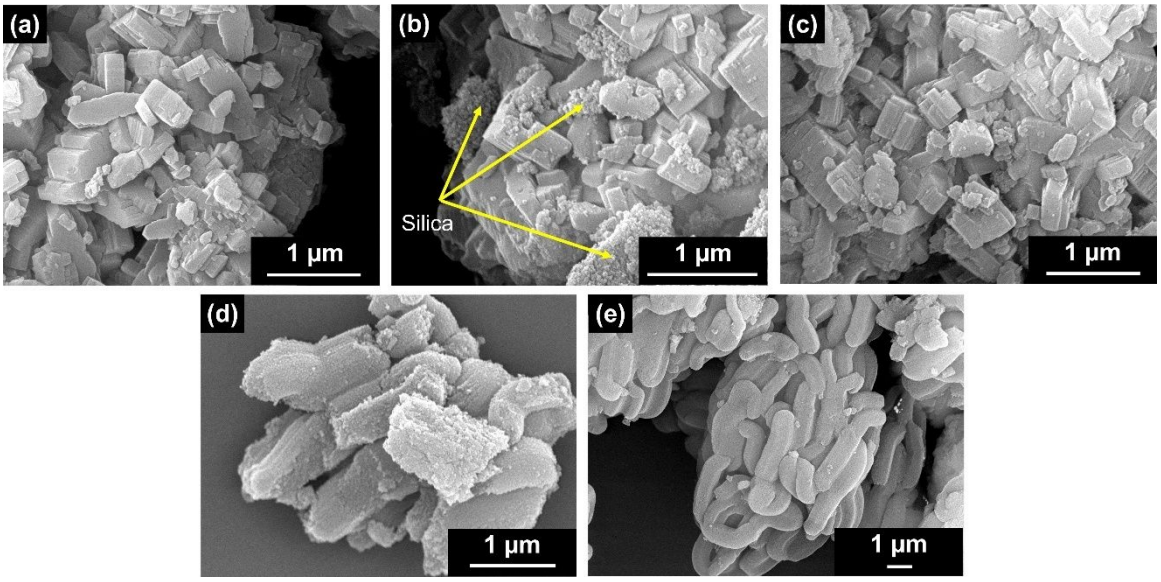

Fig. 3. SEM images of (a) ZSM-comm, (b) Meso-ZSM, (c) Mg/meso-ZSM, (d) Mg-Ni/meso-ZSM, and (e) Mg-Pt/meso-ZSM.

The SEM (**Figs. 3d** and **e**) and TEM images (**Figs. S1d** and **e**) of Mg-Ni/meso-ZSM and Mg-Pt/meso-ZSM reveal the predominantly worm-like morphology of these samples. The particle size differs between these two samples: Mg-Ni/meso-ZSM has smaller particles in the range of 1-2 µm (**Fig. 3d**), while Mg-Pt/meso-ZSM has much bigger particles ranging between 3 and 6 µm (**Fig. 3e**). The larger particle size of Mg-Pt/meso-ZSM may be directly attributed to the higher silica condensation, as seen in the XRD and ICP results. The possible reason behind the formation of the SBA-15/ZSM-5 composite is the surface acidity that zeolite provides. The protonated zeolite can attract P123 micelles and promote silica condensation.[37] More importantly, Cl^- and NO_3^- promote the hydrolysis of silica, hence creating an ideal environment for growing SBA-15. As a result of the electrostatic interaction between zeolite's acid site and P123 micelle aggregates, hydrolyzed silica begins to precipitate on the triblock polymer P123, forming the mesoporous SBA-15. Hence, this is perhaps the first Si−O−Si bond being formed between ZSM-5 and SBA-15 with a mesosized channel.

The condensation of SBA-15 favours the zeolite's acidic surface, thereby leading to the formation of the SBA-15/ZSM-5 composite.[38]

HRTEM equipped with an EDS detector was used to capture higher-quality images of the loaded metals and show the size and distribution of Ni and Pt on the surface of these catalysts (**Fig. S2**). In the case of Mg-Ni/meso-ZSM, two particle size ranges are observed: nanosized particles in between 8 and 18 nm and those in the range of 80-120 nm. In comparison, Mg-Pt/meso-ZSM displays Pt nanoparticles in the size range of 20-40 nm. Notably, Pt nanoparticles do not aggregate to form big particles (> 80 nm), as previously noticed with Ni, which may be attributed to the high surface energy. Surface energy usually increases with the decrease of particle size, causing agglomeration and sintering, which likely happen during calcination.[39] It is quite interesting to see that the metals are widely distributed in the form of nanoparticles and resist sintering. This may be due to the effective confinement of these nanoparticles by SBA-15 within its mesochannels (**Fig. S2**), thus preventing the formation of bulk aggregates.[40]

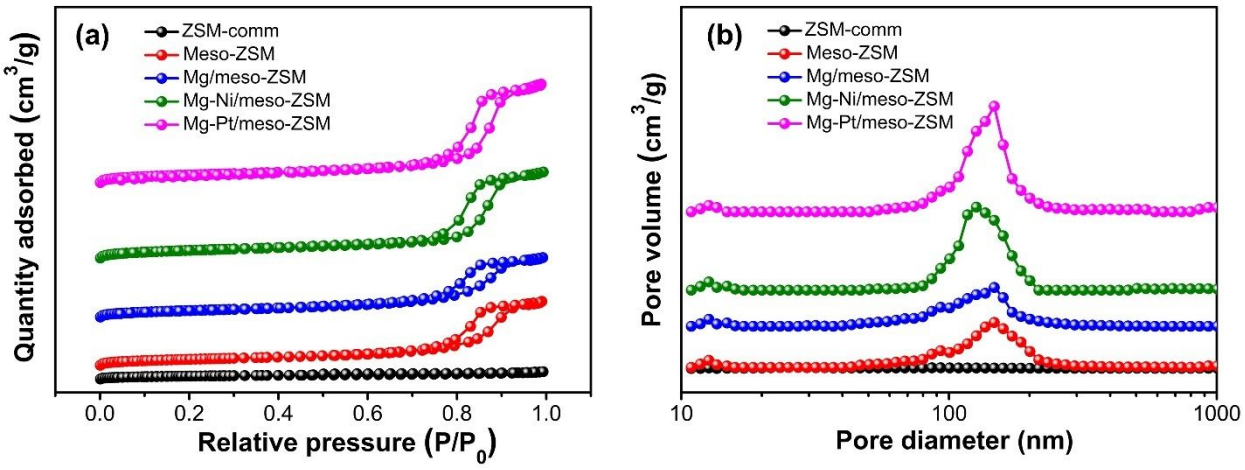

Fig. 4. (a) Nitrogen adsorption-desorption isotherms and (b) NLDFT pore size distribution of the different catalysts.

The textural properties of the samples prepared in this work are summarized in **Table 2**. The deposition of amorphous mesoporous silica on the ZSM-comm sample causes a reduction of the BET surface area from 427.8 to 365.7 m^2/g in Meso-ZSM. Similarly, Mg/meso-ZSM displays a smaller surface area than ZSM-comm. Indeed, the surface area of the amorphous silica is smaller than that of ZSM-5, thus explaining the observed reduction in surface area. In comparison, the structured framework of SBA-15 is known to have a

high surface area[41], thus justifying the higher surface areas of Mg-Ni/meso-ZSM and Mg-Pt/meso-ZSM over ZSM-comm. Except for ZSM-comm, all the samples displayed a significant amount of mesoporosity (**Table 2**). Indeed, the nitrogen adsorption-desorption isotherms in **Fig. 4a** confirm the presence of mesopores on the modified ZSM-5 samples, as evidenced by the Type IV isotherms. On the contrary, ZSM-comm exhibits a Type I isotherm, according to IUPAC classification[42], reflecting the dominant presence of micropores in this sample. Indeed, the micropore volume of ZSM-5 is 0.124 cm^3/g, while the mesopore volume is 0.021 cm^3/g.

Table 2. Textural properties of the as-prepared catalysts.

Catalyst	S_{BET} (m^2/g)	V_{micro} (cm^3/g)	V_{meso} (cm^3/g)	$D_{mesopore}$ (nm)
Comm-ZSM	427.8	0.124	0.021	N/A
Meso-ZSM	365.7	0.051	0.621	14.7
Mg/meso-ZSM	417.2	0.057	0.586	14.7
Mg-Ni/meso-ZSM	488.9	0.062	0.832	13.6
Mg-Pt/meso-ZSM	468.2	0.066	0.945	14.7

A significant decrease (~50%) in microporosity is observed for all the modified samples when compared to ZSM-comm. On the other hand, the mesoporosity rises substantially with Mg-Pt/meso-ZSM recording the highest mesoporosity (mesopore volume) of 0.945 cm^3/g, followed by Mg-Ni/meso-ZSM with 0.832 cm^3/g. The higher mesopore volume of Mg-Pt/meso-ZSM can be justified by the higher concentration of silica, *i.e.*, SBA-15, present in this sample. Additionally, the higher mesopore volumes observed over Mg-Ni/meso-ZSM and Mg-Pt/meso-ZSM compared to Meso-ZSM and Mg/meso-ZSM can be justified by the ordered structure of SBA-15 on the former samples. **Fig. 4b** shows the pore size distribution based on the DFT model, showing that all modified samples have a unimodal pore diameter distribution in the mesopore region. The biggest pore diameter of 14.7 nm is observed in Mg-Pt/meso-ZSM, which is in excellent agreement with the typical pore size of SBA-15.[41] In comparison, Mg-Ni/meso-ZSM has a slightly smaller pore diameter of 13.6 nm.

3.1.3. Acidity, basicity, and reducibility

Ammonia desorption profiles are used to study the acid density and strength of the five catalysts (**Fig. 5**). Two peaks representing weak and strong acidity are observed at $T < 200$ °C and $T \sim 400$-500 °C. As shown in **Table 3**, ZSM-comm has the highest amount of weak acidity (0.932 $mmol_{NH3}/g$) at 193 °C, and strong acidity, *i.e.*, 0.588 $mmol_{NH3}/g$ at 430 °C. The higher acidity of ZSM-comm can be directly related to this sample's low Si/Al ratio (**Table 1**). On the other hand, the rest of the modified ZSM-5 catalysts suffer a sharp reduction in weak acidity when compared to ZSM-comm. In the particular case of Meso-ZSM, the loss of weak acidity is 74%, while for the rest of the modified catalysts, the loss ranges from 34% to 55%. The observed acidity variation can be explained by the overall reduction in Al content (**Table 1**), the blockage of ZSM-5 pores by silica, ion exchange between protonic sites and Mg^{2+}, and/or partial destruction of the MFI framework during the synthesis process. In addition to the reduction of acid density, the weak acidity of the modified ZSM-5 catalysts is shifted to a lower temperature at 165 °C. This indicates that the strength of the weak acid sites on these modified catalysts is slightly lower than that on ZSM-comm.

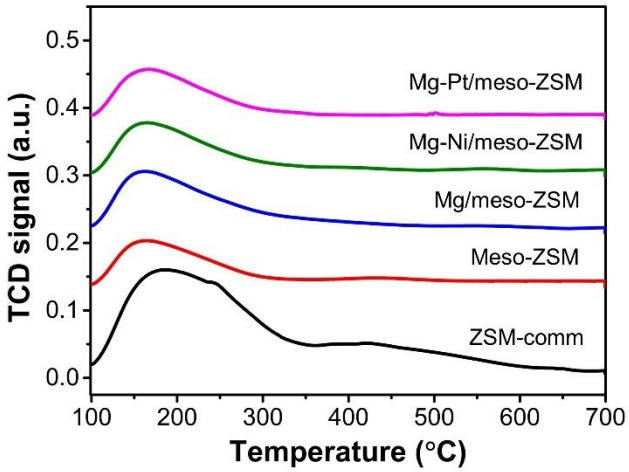

Fig. 5. NH_3-TPD profiles of commercial and modified ZSM-5 catalysts.

The strong acidity of ZSM-comm is greatly decreased from 0.588 to 0.103 mmol/g in the case of Meso-ZSM. Much like for the weak acid sites, this reduction may be explained by the deposition of silica, which decreases the overall sample's Al content and reduces the accessibility to the zeolite micropores. On the other hand, the remaining catalysts (Mg/meso-ZSM, Mg-Pt/meso-ZSM, and Mg-Ni/meso-ZSM) display very few strong acid sites (>0.02 $mmol_{NH3}/g$ – **Table 3**). The observed decline of strong acidity in these catalysts is

likely due to the presence of Mg, which can replace H^+ in the zeolite and has been reported to preferably reduce the amount of strong Brønsted sites.[43, 44]

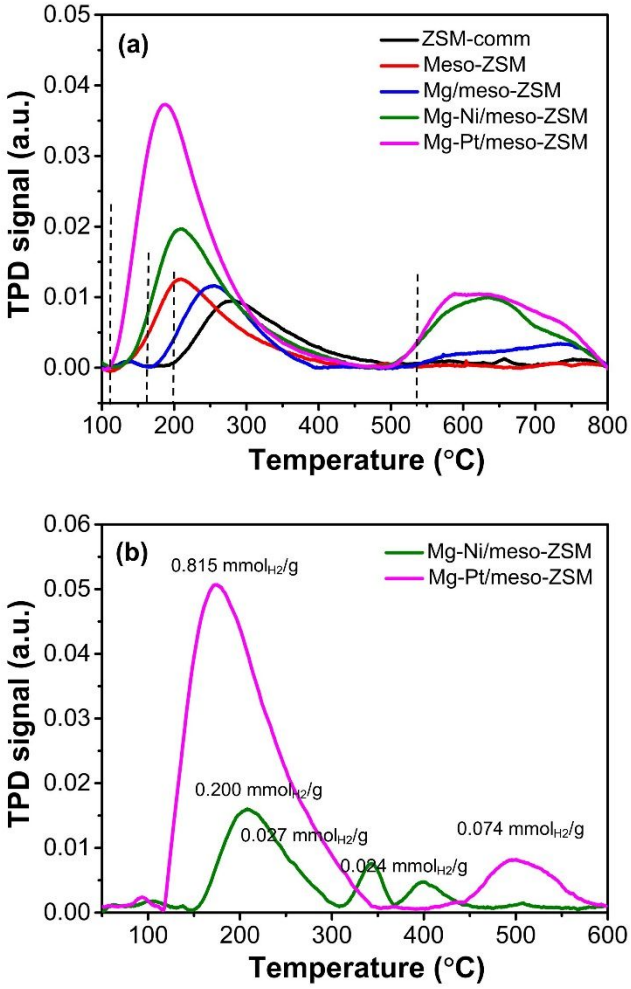

Fig. 6. (a) CO_2-TPD and (b) H_2-TPR analysis of the prepared catalysts.

The basicity of the catalysts was determined from the CO_2-TPD results shown in **Fig. 6a**. Similar to the acidity, the temperature profiles reveal the presence of two desorption peaks ascribed to weak basicity, at T = 100–400 °C, and a strong one at temperatures between 500 and 800 °C. The ZSM-comm catalyst exhibits only a weak basicity of 0.05 mmol/g at 290 °C (**Table 3**) which is the lowest among all the catalysts. While ZSM-comm is supposed to be a purely acid catalyst, the residual basicity can be attributed to trace amounts of Na in this catalyst. The incorporation of silica into Meso-ZSM leads to a slight increase in weak basicity to 0.088 and a shift in peak position to a low temperature of 210 °C. The Mg impregnation that occur before the silica growth causes the emergence of a new peak of 750 °C, assigned to strong basicity, with no noticeable effect on the number of weak basic sites. Still, a shift to 270 °C is noted, indicating that these sites are stronger

in Mg/meso-ZSM compared to Meso-ZSM and slightly weaker than ZSM-comm. The appearance of strong basic sites after Mg impregnation on zeolites has been reported by Graça *et al.*, where this strong basicity was attributed to the desorption of monodentate and bidentate carbonates attached to O^{2-} ions.[45]

Table 3. Acidity, basicity and the adsorption strength of the different catalysts.

Catalyst	Acidity (mmol NH_3/g)		Basicity (mmol CO_2/g)	
	Weak	Strong	Weak	Strong
Comm-ZSM	0.932	0.588	0.050	0.00
Meso-ZSM	0.243	0.103	0.088	0.00
Mg/meso-ZSM	0.614	0.008	0.090	0.035
Mg-Ni/meso-ZSM	0.522	0.016	0.134	0.089
Mg-Pt/meso-ZSM	0.512	0.018	0.240	0.107

The incorporation of Ni and Pt greatly boosts the weak and strong basicity simultaneously. Indeed, the addition of Pt and Ni has been reported to enhance the basicity of a catalyst.[46, 47] Mg-Pt/meso-ZSM reveals the highest weak basicity of 0.240 $mmol_{CO2}$/g followed by Mg-Ni/meso-ZSM, which has a basicity of 0.134 $mmol_{CO2}$/g. The strong basicity peaks of Mg-Pt/meso-ZSM (0.107 $mmol_{CO2}$/g) and Mg-Ni/meso-ZSM (0.089 $mmol_{CO2}$/g) are both centered at 640 °C with an additional shoulder peak at 750 °C that is likely associated to Mg, as it coincides with the peak observed on Mg/meso-ZSM. Therefore, the strong basicity of these two catalysts is a combination of the basicity formed by Mg and Ni/Pt. It is important to mention that the basicity of Mg-Ni/meso-ZSM and Mg-Pt/meso-ZSM is significantly higher than that of Mg/meso-ZSM despite the lower Mg loading, *i.e.*, 0.37 wt.% versus 0.21 wt.% and 0.19 wt.%, respectively. Thus, the observed excess of basic sites must be attributed to the presence of Ni and Pt.

To further investigate the effect of incorporating Ni and Pt and their potential roles in the reaction, the catalysts were analyzed by H_2-TPR to identify their reduction temperatures and oxidation states within the catalyst structure. As shown in **Fig. 6b**, the Mg-Ni/meso-ZSM catalyst shows three reduction peaks at 215 °C, 345°C, and 400 °C. Usually, Ni exhibits a reducibility behaviour at relatively high temperatures, however,

there are few cases where it can be reduced at low temperatures. The peak at the lowest temperature (215 °C), represents the Ni species with weak interaction with the support, which probably means that the Ni in this state is in bulk NiO form.[48-50] However, other studies have assigned this peak to Ni_2O_3.[51, 52] The second reduction peak at 345 °C, is an indication of small or highly dispersed NiO clusters.[53] Lastly, the third reduction peak at 400 °C, indicates a strong metal-support interaction[54], typically attributed to the positioning of Ni within the mesoporosity.[55] Instead of three reduction peaks, the Mg-Pt/meso-ZSM catalyst only develops two main H_2 consumption peaks at 180 and 500 °C. Comparable to Mg-Ni/meso-ZSM, the reduction peak at low temperatures is assigned to Pt^{2+}, which is attributed to the weak metal-silica interaction.[56] On the contrary, the high H_2 consumption peak at 500 °C confirms the formation of strong Pt-silica interaction, hence proving the existence of Pt^{4+} species.[57]

The activity and accessibility of metals are primarily dependent on their location. X-ray photoelectron spectroscopy (XPS) was conducted in this study on Mg-Ni/meso-ZSM and Mg-Pt/meso-ZSM (as shown in **Fig. S3**) to explore these aspects further. The absence of detectable Ni on the surface of Mg-Ni/meso-ZSM may be due to the low Ni content. In contrast, there is a clear evidence of Pt (Pt 4f) on the surface of Mg-Pt/meso-ZSM based on the XPS analysis, with three major peaks observed. The peaks at 72.1 eV and 75.2 eV correspond to Pt^{2+}, while the peaks at 74.8 eV and 77.5 eV are attributed to Pt^{4+}.[58] From the XPS analysis, the proportions of Pt^{2+} and Pt^{4+} are estimated to be 61.8 at% and 38.2 at.%, respectively. These results are consistent with the H_2-TPR analysis, which indicates that Pt^{2+} is the dominant state in this sample.

Since Ni is not clearly detected through XPS analysis, UV-vis diffuse reflectance spectroscopy (DRS) was employed to study the position of nickel in the SBA-15/ZSM composite. The results (**Fig. S4**) reveal the presence of a broad absorption band in the range of 340-380 nm, which is associated with octahedral Ni^{2+} species in the NiO lattice.[59, 60] This observation matches well with the H_2-TPR analysis, confirming the formation of a weakly connected NiO lattice to the SiO_2 structure. The low peak intensity implies the low Ni content in this sample, and no evidence of tetrahedrally coordinated Ni^{2+} species is found in the 550 to 650 nm region.[60]

Further examination was conducted using FTIR to determine the environment around Mg species, as given in **Fig S5**. The Mg concentration is also not high as it reaches a maximum of 0.37 wt.% in Mg/meso-

ZSM. In spite of that, the presence of Mg is confirmed by the absorption peak observed at 435 cm^{-1}. This peak emerges only in Mg-containing samples (**Fig. S5**) and can be ascribed to Mg−O stretching vibration according to previous reports.[61, 62] This peak may originate from either $Mg(OH)_2$ or MgO. However, as the calcination step was performed after the catalyst synthesis, this rules out the possibility of having $Mg(OH)_2$. Interestingly, both Mg-Ni/meso-ZSM and Mg-Pt/meso-ZSM exhibit an additional peak that may be directly linked to the addition of Ni and Pt into these samples. The peak situated at 1382 cm^{-1} is usually assigned to carbonate species[63], indicating the formation of $Ni(CO_3)_2$ and $Pt(CO_3)$ over these two samples. The appearance of this peak despite the overnight drying of all samples before the analysis suggests that CO_2 from the environment may form a strong bond with the metals, which coincides with the CO_2-TPD result.

3.2. Co-pyrolysis of pinewood and polyethylene

Thermal pyrolysis was used as a baseline to evaluate the impact of the different catalysts. Without a catalyst (non-cat), the total condensate yield, which includes the organic liquid (oil), water in liquid (water), and condensed solid products (wax), reaches 62 wt.%, as shown in **Fig. 7**. It is worth noticing that the highest oil and wax yields are obtained when no catalyst is present (**Fig. 7**). In contrast, ZSM-comm gives the lowest oil yield of 4.9 wt.%, and the highest gas yield of 50.4%, indicating excessive cracking. The high gas yield observed for ZSM-comm is in agreement with the larger acid site density observed in this sample, particularly the strong acid sites (**Table 3**). Despite the low oil yield, the wax yield is 14 wt.%, which is relatively high considering that polyethylene (PE) is the main contributor to this product formation and represents 20 wt.% of the feedstock. This suggests that ZSM-comm is not effective at cracking the wax products from PE into oil or gas products. The incapacity of ZSM-comm to efficiently promote the conversion of PE can be explained by the higher affinity of zeolites' active sites toward the oxygenated products produced from biomass pyrolysis, which can hinder the conversion of the less reactive hydrocarbon products from PE pyrolysis.[64, 65] Indeed, in the absence of biomass, the commercial ZSM-5 zeolite (ZSM-comm) efficiently converts PE into gas and oil products.[66] Concerning the quality of the oil (**Fig. 8**), 67.5% appears in the form of aromatic hydrocarbons and 7.6% as alkanes and alkenes, making the total oxygenates in this sample only 25%. While

the concentration of hydrocarbons in the oil phase is substantial, the oil yield obtained with ZSM-comm is only 4.9 wt.%, thus the feedstock conversion into liquid hydrocarbons is minimal.

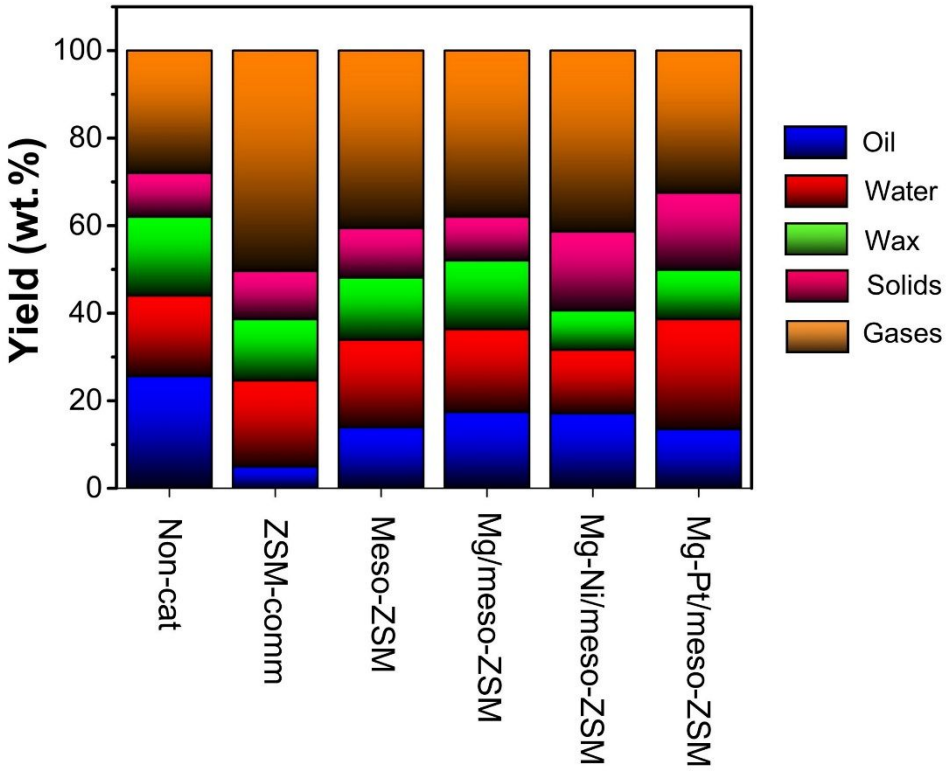

Fig. 7. Co-pyrolysis product yield over different catalysts.

The introduction of mesoporous silica (SBA-15) dramatically changes the catalytic performance of zeolite as Meso-ZSM yields 13.9 wt.% of oil, almost threefold that of ZSM-comm, while maintaining a similar yield of water (20 wt.%), wax (14 wt.%), and solid (11 wt.%) and producing less gas (40 wt.%) (**Fig. 8**). However, the oxygenate selectivity is increased to 77.8%, which can be explained by the significant reduction in acidity of this sample when compared to ZSM-comm. On the other hand, comparing the Meso-ZSM and Non-cat performance clearly illustrates the ability of this catalyst to convert sugar compounds (17.3% in Non-cat) into carboxylic acids and ketones as the selectivity climbs by 15.4 and 27.3%, respectively (**Fig. 8**).

The impregnation of Mg enhances the oil yield further as it reaches 17.4% over Mg/meso-ZSM (**Fig. 7**). This enhancement is accompanied by a slight increase in alkanes and alkenes selectivity from 3.2 to 7.1% compared with Meso-ZSM (**Fig. 8**). The increment may be caused by the role of Mg in facilitating PE cracking.[67] Meanwhile, the significant increase in oil yield can be linked to the suppression of strong acidity,

which is responsible for severe cracking and the introduction of strong base sites, which can promote condensation and deoxygenation.

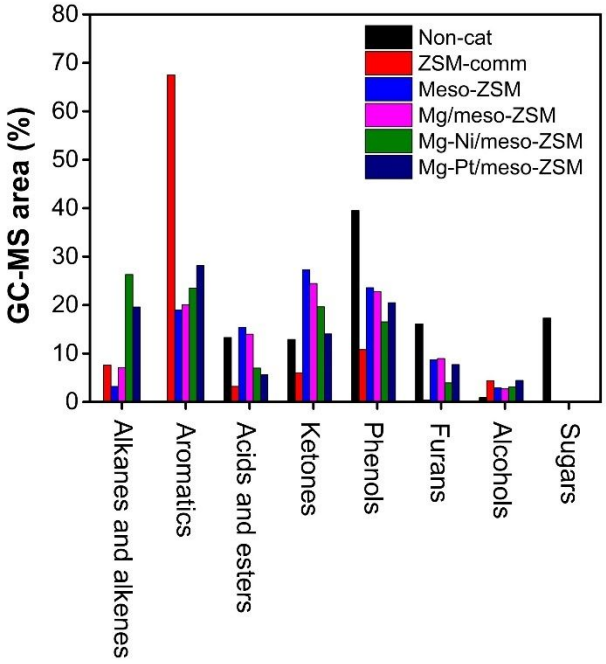

Fig. 8. Co-pyrolysis product distribution based on GC-MS results.

The yield of the non-condensable gases for the different catalysts is shown in **Fig. 9**. Independently of the catalyst (Non-cat), CO is the main gas product followed by CO_2. ZSM-comm is the catalyst with the highest gas yield, with CO yield representing 33.8 wt.% and CO_2 10.8 wt.%. On the other hand, CO yield significantly decreases over Mg-Ni/meso-ZSM and Mg-Pt/meso-ZSM to 22.1 and 18.2%, respectively. This indicates that the trifunctional catalysts can minimize the decarbonylation pathway. In contrast, Mg-Ni/meso-ZSM and Mg-Pt/meso-ZSM exhibit higher selectivity to CO_2 than ZSM-comm (**Fig. 9**), suggesting that these catalysts favour decarboxylation and reactions, such as acids ketonization, which also releases CO_2, as confirmed by the reduction in carboxylic acids in the oil. It should be mentioned that the elimination of oxygen as CO_2 is more favourable for minimizing carbon losses and maximizing carbon recovery than CO. Moreover, reactions like ketonization can help to maximize the products in the fuel range.

The incorporation of Ni and Pt into the catalysts significantly changes the catalytic performance of Meso-ZSM. The Mg-Ni/meso-ZSM and Mg-Pt/meso-ZSM catalysts maintain high oil yields of 17.1 and 13.5 wt.%, respectively (**Fig. 7**), while the hydrocarbon content in the oil phase greatly increases when compared

to Mg/meso-ZSM. The hydrocarbon alkanes and alkenes in the liquid correspond to 26.3 wt.% on Mg-Ni/meso-ZSM and 19.6 wt.% on Mg-Pt/meso-ZSM, up from only 7.1 wt.% when no Ni or Pt is present (Mg/meso-ZSM), as seen in **Fig. 8**. The rise in hydrocarbon alkanes and alkenes is likely associated with the drop in wax yield from 15.7 wt.% to 9 wt.% and 11 wt.% on Mg-Ni/meso-ZSM and Mg-Pt/meso-ZSM, respectively (**Fig. 7**). Thus, the introduction of Ni and Pt into Meso-ZSM catalyst enables a more efficient conversion of PE. This observation can be explained by the capacity of the metal sites to promote the wax hydrogenolysis[68], and the transfer of hydrogen from the wax into the biomass pyrolysis intermediates promoted by the metal sites, which reduce their affinity with the zeolite acid sites, thereby enabling a more effective cracking of the wax. The formation of aromatic hydrocarbons is a side effect of the hydrogen transfer reaction, and the contribution of these compounds to the oil composition increases from 20.1% in Mg/meso-ZSM to 23.5% and 28.2% in Mg-Ni/meso-ZSM and Mg-Pt/meso-ZSM, respectively (**Fig. 8**). Similarly, if hydrogen is being transferred to biomass pyrolysis intermediates, the contribution of H_2O as a deoxygenation product is expected to increase. While this is observed over Mg-Pt/meso-ZSM, where the water yield is 25 wt.% compared to 18.9 wt.% over Mg/meso-ZSM and 20% over Meso-ZSM, the opposite is observed on Mg-Ni/meso-ZSM (water yield = 14.5 wt.%) (**Fig. 7**). Therefore, the increase of hydrocarbons in Mg-Ni/meso-ZSM oil phase has a higher contribution of hydrogenolysis, while in Mg-Pt/meso-ZSM, hydrogen transfer seems to dominate. Indeed, the capacity of Ni to promote C−C bond cleavage is much higher than that of Pt[69], and the higher contribution of light hydrocarbons to the Mg-Ni/meso-ZSM gas yield also agrees with the higher occurrence of hydrogenolysis in this sample.

In terms of oxygenated products in the oil, when Pt and Ni are present in the catalyst, the carboxylic acid selectivity is reduced from 14% in Mg/meso-ZSM to 7% and 5.6% in Mg-Ni/meso-ZSM and Mg-Pt/meso-ZSM, respectively (**Fig. 8**). Moreover, the occurrence of ketones also declines significantly. The reduction of carboxylic acids can be explained by the higher density of weak and strong base sites in Mg-Ni/meso-ZSM and Mg-Pt/meso-ZSM, which is known to promote the ketonization route of acids to ketones, explaining the decline in selectivity toward acids.[70] Ketones can be easily converted on base and acid sites through aldol condensation and are also susceptible to hydrogenation via hydrogen transfer. These phenomena account for the lower occurrence of ketones and acids on Mg-Pt/meso-ZSM, which displays higher basicity

(**Table 3**) and capacity for hydrogen transfer. Finally, the ability of Mg-Ni/meso-ZSM to crack PE to short chain alkenes and the decrease in selectivity toward furans (from 9.0% to 3.9%, **Fig. 8**) observed with this sample indicates the occurrence of the Diels-Alder reaction. The increase in aromatic selectivity is another indication of the validity of this hypothesis.

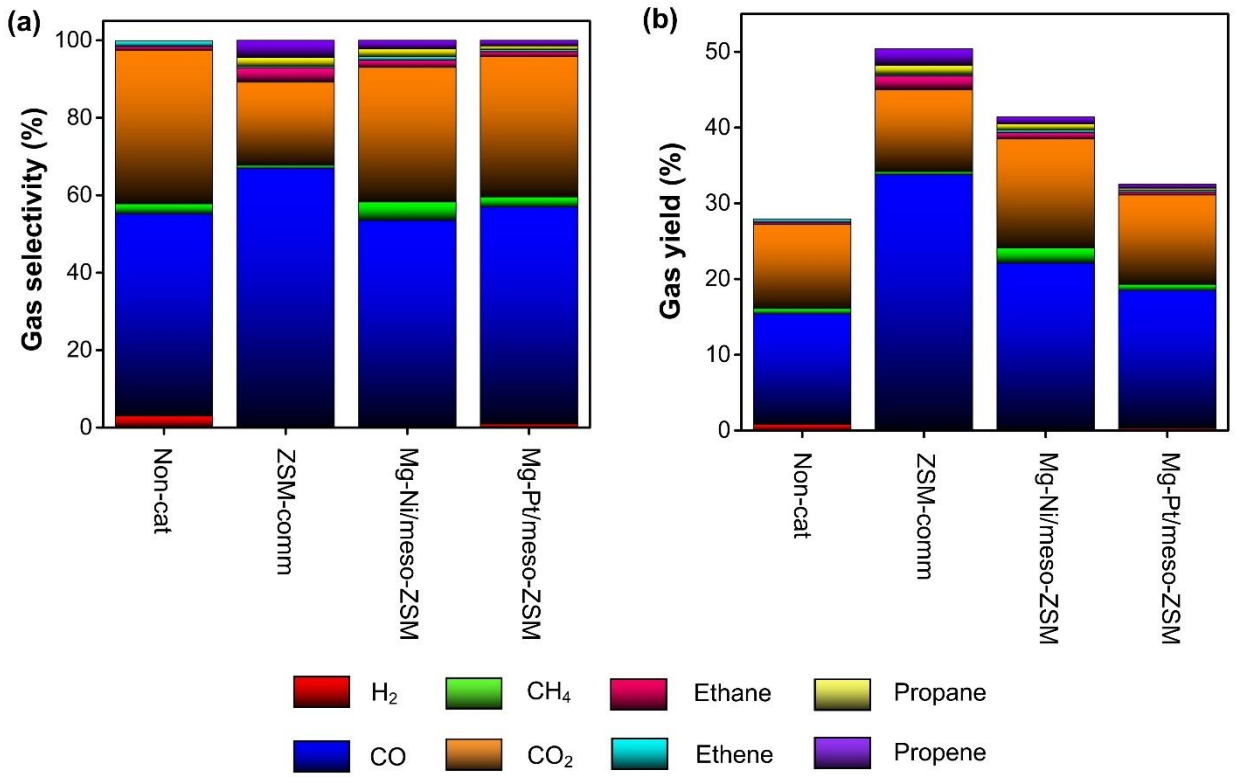

Fig. 9. GC-TCD results of non-condensable gases collected during the co-pyrolysis process.

The above results suggest that the trifunctional catalysts (Mg-Ni/meso-ZSM and Mg-Pt/meso-ZSM) maximize the yield of hydrocarbons in the oil fraction by increasing wax conversion and favouring deoxygenation. This performance enables a significant portion of carbon from the feedstock to be retained in the oil, particularly when compared to ZSM-comm. Furthermore, the reduction in acidity by incorporating silica and Mg prevents excessive cracking, *i.e.*, lowers gas formation. Additionally, the presence of a base site favours condensation reactions, thus increasing the oil yield and assisting with deoxygenation. Finally, the Ni in Mg-Ni/meso-ZSM is found to promote the C−C cleavage of wax products by incorporating them into the oil. On the other hand, the Pt in Mg-Pt/meso-ZSM favours hydrogen transfer between the wax and the oxygenates, improving oxygen elimination by H_2O removal.

3.3. Coke deposition and diffusion obstruction

The deactivation of catalysts in biomass pyrolysis is typically due to diffusion limitations caused by rapid coke formation. To assess the impact of coke loading on catalyst porosity, the spent catalysts were analyzed by BET and thermogravimetric analysis (TGA) measurements. The TGA profiles in **Fig. S6** show that all samples experience a weight loss of 2-4 wt.% at low temperatures. This is likely due to the removal of moisture and adsorbed gases. This weight loss is not included in the calculation of the coke amount, which is limited to the weight loss observed from 250 °C to 800 °C. The spent ZSM-comm catalyst has a high coke loading of 6.8 wt.% (**Table S1**), which can be directly attributed to the high number of strong acid sites. As a result, the surface area of the catalyst decreases from 427.8 to 21.7 m^2/g, indicating that this highly acidic microporous catalyst is not suitable for biomass pyrolysis. The spent Meso-ZSM catalyst has less coke deposition with a coke loading of 5.9 wt.%, which may be caused by the introduction of mesoporosity and the reduction in the number of strong acid sites. This positively impacts the surface area of the spent catalyst, which is only decreased to 132.2 m^2/g. Interestingly, the spent Mg/meso-ZSM catalyst has the same coke loading of 5.9 wt.%, but maintains a high surface area of 253.2 m^2/g. This may be due to the higher surface area of fresh Mg/meso-ZSM and the lower number of strong acid sites. The samples containing SBA-15, Mg-Ni/meso-ZSM and Mg-Pt/meso-ZSM, behave differently due to the nature of the SBA-15 channel, which is composed of straight cylindrical tubes. The spent Mg-Ni/meso-ZSM sample has the highest coke loading of 7.0 wt.%, but with a much lower surface area than Mg/meso-ZSM (only 123.7 m^2/g). The same observation is noted for the spent Mg-Pt/meso-ZSM catalyst as the surface area also drops to 134.9 m^2/g. This may be attributed to the long, one-dimensional cylindrical channels of SBA-15, which can be easily blocked at the pore entrance, making the entire channel inaccessible. Additionally, the shape of the hysteresis loop of the spent Mg-Ni/meso-ZSM and Mg-Pt/meso-ZSM changes from a H2(a) type to a H2(b) type, suggesting that the width of the pore mouth becomes narrower due to coke deposition, as shown in **Fig. S7**.[71]

4. Conclusions

A trifunctional catalyst with acid, base, and metal functions has been synthesized from a commercial ZSM-5 zeolite. The composite materials are composed of mesoporous silica (SBA-15) where the metal (Ni or Pt)

nanoparticles are deposited and commercial ZSM-5 with acid and base sites. The interaction of the three active sites is exploited to upgrade the vapours from the co-pyrolysis of pinewood (80 wt.%), and polyethylene (20 wt.%). The presence of the three types of active sites leads to a significant increase in oil yield from 4.9 wt.% in commercial ZSM-5 (ZSM-comm) to 17 wt.% in Mg-Ni/meso-ZSM, while enriching this fraction in linear hydrocarbons. The mild acidity and stronger basicity of Mg-Ni/meso-ZSM and Mg-Pt/meso-ZSM reduce overcracking and favour condensation reactions. Furthermore, the metal sites on the meso-ZSM promote the hydrogen transfer between the wax fraction from PE (Mg-Pt/meso-ZSM) and the C−C cleavage of the large paraffins in wax (Mg-Ni/meso-ZSM). Thisincreases the occurrence of hydrocarbons in the oil and promoting hydrogenation. Finally, Mg-Ni/meso-ZSM exhibits excellent performance in promoting the Diels-Alder reaction between furans and olefins, resulting in more aromatics. This study demonstrates the significance of rational catalyst design in the transformation of complicated feedstocks, such as pyrolysis vapours. To improve the quality of pyrolysis bio-oil and facilitate its transformation into fuels, an advanced catalyst pore system consisting of micro- and mesopore channels that facilitate the accessibility of reaction products and a variety of active sites capable of promoting multiple types of reactions is required.

Acknowledgments

The authors acknowledge the Queensland node of Metabolomics Australia (Q-MAP) at The University of Queensland, an NCRIS initiative under Bioplatforms Australia Pty Ltd. M. K. acknowledges Advance Queensland Fellowship scheme. Y. V. K. acknowledges the funding from the Queensland government through the Advance Queensland Fellowship Program (AQIRF043-2020-CV). Y. Y and Y. V. K. are grateful for the financial support given by JST through the ERATO Program (JPMJER2003). M. K. and Y. V. K. thank the Australian Research Council for the financial support provided through the Linkage Project scheme (ARC LP190100849). M. R. K. and I. A. A. extend their appreciation to the Researchers Supporting Project number (RSPD2023R597), King Saud University, Riyadh, Saudi Arabia. This work was performed in part at the Queensland node of the Australian National Fabrication Facility (ANFF), a company established under the

National Collaborative Research Infrastructure Strategy to provide nano and microfabrication facilities for Australia's researchers.

References

1. K. Moustakas, M. Loizidou, M. Rehan and A. S. Nizami, *Renew. Sustain. Energy Rev.*, 2020, **119**, 109418.
2. A. Rong and R. Lahdelma, *Renew. Sustain. Energy Rev.*, 2016, **53**, 363-372.
3. L. Chand Malav, K. K. Yadav, N. Gupta, S. Kumar, G. K. Sharma, S. Krishnan, S. Rezania, H. Kamyab, Q. B. Pham, S. Yadav, S. Bhattacharyya, V. K. Yadav and Q.-V. Bach, *J. Cleaner Prod.*, 2020, **277**, 123227.
4. A. Kumar and S. R. Samadder, *Waste Manag.*, 2017, **69**, 407-422.
5. A. P. Pinheiro Pires, J. Arauzo, I. Fonts, M. E. Domine, A. Fernández Arroyo, M. E. Garcia-Perez, J. Montoya, F. Chejne, P. Pfromm and M. Garcia-Perez, *Energy Fuels*, 2019, **33**, 4683-4720.
6. P. T. Williams and N. Nugranad, *Energy*, 2000, **25**, 493-513.
7. M. M. Rahman, R. Liu and J. Cai, *Fuel Proc. Technol.*, 2018, **180**, 32-46.
8. M. H. Ahmed, N. Batalha, H. M. Mahmudul, G. Perkins and M. Konarova, *Biores. Technol.*, 2020, 123457.
9. H. Hernando, A. M. Hernández-Giménez, C. Ochoa-Hernández, P. C. Bruijnincx, K. Houben, M. Baldus, P. Pizarro, J. M. Coronado, J. Fermoso and J. Čejka, *Green Chem.*, 2018, **20**, 3499-3511.
10. C. Liu, H. Wang, A. M. Karim, J. Sun and Y. Wang, *Chem. Soc. Rev.*, 2014, **43**, 7594-7623.
11. E. Saraçoğlu, B. B. Uzun and E. Apaydın-Varol, *Int. J. Hydrog. Energy*, 2017, **42**, 21476-21486.
12. R. Liu, M. Sarker, M. M. Rahman, C. Li, M. Chai, Nishu, R. Cotillon and N. R. Scott, *Prog. Energy Combust. Sci.*, 2020, **80**, 100852.
13. W. Wang, R. Lemaire, A. Bensakhria and D. J. J. o. A. Luart, *J. Anal. Appl. Pyrolysis*, 2022, 105479.
14. L. Fan, P. Chen, Y. Zhang, S. Liu, Y. Liu, Y. Wang, L. Dai and R. Ruan, *Biores. Technol.*, 2017, **225**, 199-205.
15. X. Chen, Q. Che, S. Li, Z. Liu, H. Yang, Y. Chen, X. Wang, J. Shao and H. Chen, *Fuel Proc.Technol.*, 2019, **196**, 106180.
16. K. Ding, Z. Zhong, J. Wang, B. Zhang, L. Fan, S. Liu, Y. Wang, Y. Liu, D. Zhong and P. Chen, *Biores. Technol.*, 2018, **261**, 86-92.
17. I. Graça, M. C. Bacariza and D. Chadwick, *Microporous Mesoporous Mater.*, 2018, **255**, 130-139.
18. K. Wang, M. Dong, X. Niu, J. Li, Z. Qin, W. Fan and J. Wang, *Catalysis Science Technology*, 2018, **8**, 5646-5656.
19. H. W. Lee, J. S. Cha and Y.-K. Park, *Catalysts*, 2018, **8**, 506.
20. H. W. Ryu, D. H. Kim, J. Jae, S. S. Lam, E. D. Park and Y.-K. Park, *Biores. Technol.*, 2020, **310**, 123473.

21. E. F. Iliopoulou, S. D. Stefanidis, K. G. Kalogiannis, A. Delimitis, A. A. Lappas and K. S. Triantafyllidis, *Appl. Catal. B*, 2012, **127**, 281-290.
22. A. C. Dyer, M. A. Nahil and P. T. Williams, *J. Mater. Cycles Waste Manag.*, 2022, **24**, 477-490.
23. N. Miskolczi, T. Juzsakova and J. Sója, *J. Energy Inst.*, 2019, **92**, 118-127.
24. L. Jia, M. Raad, S. Hamieh, J. Toufaily, T. Hamieh, M. Bettahar, G. Mauviel, M. Tarrighi, L. Pinard and A. Dufour, *Green Chem.*, 2017, **19**, 5442-5459.
25. M. H. Ahmed, N. Batalha, Z. A. Al-Othman, Y. Yamauchi, Y. V. Kaneti and M. Konarova, *Chem. Eng. J.*, 2021, 132965.
26. M. H. M. Ahmed, N. Batalha, J. Xu, Y. Yamauchi and M. Konarova, *Microporous Mesoporous Mater.*, 2022, **330**, 111579.
27. H. Shafaghat, H. W. Lee, Y. F. Tsang, D. Oh, J. Jae, S.-C. Jung, C. H. Ko, S. S. Lam and Y.-K. Park, *Chem. Eng. J.*, 2019, **366**, 330-338.
28. P. S. Rezaei, D. Oh, Y. Hong, Y.-M. Kim, J. Jae, S.-C. Jung, J.-K. Jeon and Y.-K. Park, *Energy Convers. Manag.*, 2017, **151**, 116-122.
29. Y.-M. Kim, H. W. Lee, J. Jae, K. B. Jung, S.-C. Jung, A. Watanabe and Y.-K. Park, *Catal. Today*, 2017, **298**, 46-52.
30. C. Flores, V. L. Zholobenko, B. Gu, N. Batalha, V. Valtchev, W. Baaziz, O. Ersen, N. R. Marcilio, V. V. Ordomsky and A. Y. Khodakov, *ACS Appl. Nano Mater.*, 2019, **2**, 4507-4517.
31. C. Flores, N. Batalha, V. V. Ordomsky, V. L. Zholobenko, W. Baaziz, N. R. Marcilio and A. Y. Khodakov, *ChemCatChem*, 2018, **10**, 2291-2299.
32. W. Wang, J. Zhao, Y. Xu, C. Zhang, W. Shan, D. Nguyen and H. Ru, *RSC Adv.*, 2014, **4**, 2195-2204.
33. Z. Luan, M. Hartmann, D. Zhao, W. Zhou and L. Kevan, *Chem. Mater.*, 1999, **11**, 1621-1627.
34. C.-m. Yang, P.-h. Liu, Y.-f. Ho, C.-y. Chiu and K.-j. Chao, *Chem. Mater.*, 2003, **15**, 275-280.
35. M. H. M. Ahmed, O. Muraza, A. M. Al-Amer and Z. H. Yamani, *Microporous Mesoporous Mater.*, 2016, **227**, 48-56.
36. A. Abraham, S.-H. Lee, C.-H. Shin, S. B. Hong, R. Prins and J. A. van Bokhoven, *Phys. Chem. Chem. Phys.*, 2004, **6**, 3031-3036.
37. E. Leontidis, *Curr. Opin. Colloid Interface Sci.*, 2002, **7**, 81-91.
38. X. Qian, J. Du, B. Li, M. Si, Y. Yang, Y. Hu, G. Niu, Y. Zhang, H. Xu and B. Tu, *Chem. Sci.*, 2011, **2**, 2006-2016.
39. R. H. Castro and D. Gouvêa, *J. Am. Chem. Soc.*, 2016, **99**, 1105-1121.
40. A. Ungureanu, B. Dragoi, A. Chirieac, S. Royer, D. Duprez and E. Dumitriu, *J. Mater. Chem.*, 2011, **21**, 12529-12541.
41. M. Kruk, M. Jaroniec, C. H. Ko and R. Ryoo, *Chem. Mater.*, 2000, **12**, 1961-1968.
42. K. S. Sing and R. T. Williams, *Adsorp. Sci. Technol.*, 2004, **22**, 773-782.
43. Y.-G. Li, W.-H. Xie and S. Yong, *Appl. Catal. A*, 1997, **150**, 231-242.

44. C. Chen, Q. Zhang, Z. Meng, C. Li and H. Shan, *Appl. Petrochem. Res.*, 2015, **5**, 277-284.
45. I. Graça, M. C. Bacariza, A. Fernandes and D. Chadwick, *Appl. Catal. B*, 2018, **224**, 660-670.
46. X. Guo, A. Traitangwong, M. Hu, C. Zuo, V. Meeyoo, Z. Peng and C. Li, *Energy Fuels*, 2018, **32**, 3681-3689.
47. A. Efremova, I. Szenti, J. Kiss, Á. Szamosvölgyi, A. Sápi, K. Baán, L. Olivi, G. Varga, Z. Fogarassy and B. Pécz, *Appl. Surf. Sci.*, 2022, **571**, 151326.
48. V. Mohan, C. Raghavendra, C. V. Pramod, B. D. Raju and K. S. R. Rao, *RSC Adv.*, 2014, **4**, 9660-9668.
49. A. Cárdenas-Arenas, A. Quindimil, A. Davó-Quiñonero, E. Bailón-García, D. Lozano-Castelló, U. De-La-Torre, B. Pereda-Ayo, J. A. González-Marcos, J. R. González-Velasco and A. Bueno-López, *Appl. Catal. B*, 2020, **265**, 118538.
50. P. Yan, M. M.-J. Li, E. Kennedy, A. Adesina, G. Zhao, A. Setiawan and M. J. Stockenhuber, *Catal. Sci. Technol.*, 2020, **10**, 810-825.
51. Y. Wu, B. Wu, Y. He and T. Wu, *Chem. Lett.*, 2009, **38**, 284-285.
52. B. Mile, D. Stirling, M. A. Zammitt, A. Lovell and M. Webb, *J. Catal.*, 1988, **114**, 217-229.
53. Z.-P. Hu, C.-C. Weng, C. Chen and Z.-Y. Yuan, *Appl. Catal. A*, 2018, **562**, 49-57.
54. M. M. Yung, A. K. Starace, C. Mukarakate, A. M. Crow, M. A. Leshnov and K. A. Magrini, *Energy Fuels*, 2016, **30**, 5259-5268.
55. W. Li, H. Wang, X. Wu, L. E. Betancourt, C. Tu, M. Liao, X. Cui, F. Li, J. Zheng and R. Li, *Fuel*, 2020, **274**, 117859.
56. M. Sun, S. Wang, Y. Li, Q. Wang, H. Xu and Y. Chen, *J. Taiwan Inst. Chem. Eng.*, 2017, **78**, 401-408.
57. J. Wang, X. Guo, Y. Shi and R. Zhou, *J. Environ. Sci.*, 2021, **107**, 87-97.
58. Y. Dong, Y. Wang, Z. Tian, K. Jiang, Y. Li, Y. Lin, C. W. Oloman, E. L. Gyenge, J. Su and L. Chen, *Innov.*, 2021, **2**, 100161.
59. S. A. Karakoulia, E. Heracleous and A. A. Lappas, *Catal. Today*, 2020, **355**, 746-756.
60. M. Popova, P. Djinović, A. Ristić, H. Lazarova, G. Dražić, A. Pintar, A. M. Balu and N. Novak Tušar, *Front. Chem.*, 2018, **6**, 285.
61. I. W. Sutapa, A. W. Wahab, P. Taba and N. La Nafie, *Orient. J. Chem.*, 2018, **34**, 1016.
62. M. Rezaei, M. Khajenoori and B. Nematollahi, *Powder Technol.*, 2011, **205**, 112-116.
63. C. Rincke, S. Bette, R. E. Dinnebier and W. Voigt, *Euro. J. Inorg. Chem.*, 2015, **2015**, 5913-5920.
64. I. Graça, J. Lopes, M. Ribeiro, F. R. Ribeiro, H. Cerqueira and M. De Almeida, *Appl. Catal. B*, 2011, **101**, 613-621.
65. I. Graça, F. R. Ribeiro, H. Cerqueira, Y. Lam and M. De Almeida, *Appl. Catal. B*, 2009, **90**, 556-563.
66. M. M. Hasan, N. Batalha, G. Fraga, M. H. Ahmed, L. Pinard, M. Konarova, S. Pratt and B. Laycock, *Sustain. Energy Fuels*, 2022, **6**, 1587-1602.

67. J. Weng, C. Cui, Z. Zhou, Y. Zhang, Z. Cheng and J. Pan, *Biores. Technol.*, 2021, **338**, 125560.
68. D. W. Flaherty, D. D. Hibbitts and E. Iglesia, *J. Am. Chem. Soc.*, 2014, **136**, 9664-9676.
69. A. Almithn and D. Hibbitts, *J. Phys. Chem. C*, 2019, **123**, 5421-5432.
70. S. Gea, K. Wijaya, A. Nadia, A. N. Pulungan and J. L. Sihombing, *Int. J. Energy Environ. Eng.*, 2022, **13**, 541-553.
71. M. Thommes, K. Kaneko, A. V. Neimark, J. P. Olivier, F. Rodriguez-Reinoso, J. Rouquerol and K. S. Sing, *Pure Appl. Chem.*, 2015, **87**, 1051-1069.